Insight into the mechanism of the water–gas shift reaction over Au/CeO$_2$ catalysts using combined *operando* spectroscopies

Marc Ziemba[1], M. Verónica Ganduglia-Pirovano[2], Christian Hess[1*]

[1]Eduard-Zintl-Institut für Anorganische und Physikalische Chemie, Technische Universität Darmstadt, Alarich-Weiss-Str. 8, 64287 Darmstadt, Germany

*christian.hess@tu-darmstadt.de

[2]Instituto de Catálisis y Petroleoquímica – Consejo Superior de Investigaciones Científicas, Marie Curie 2, 28049 Madrid, Spain

Keywords

Abstract

The mechanism of the low-temperature water–gas shift (LT-WGS) reaction over Au/CeO_2 catalysts with different ceria terminations, i.e., (111), (110), and (100) facets, was investigated. Using combined *operando* Raman and UV-Vis spectroscopy as well as isotope exchange experiments, we are able to draw conclusions about the reducibility behaviour and the exchange of surface oxygen. Additional density functional theory (DFT) calculations facilitate the vibrational bands assignments and enhance the interpretation of the results on a molecular level. A facet-dependent role of gold is observed with respect to the oxygen dynamics, since for the $CeO_2(111)$ facet the presence of gold is required to exchange surface oxygen, whereas the $CeO_2(110)$ facet requires no gold, as rationalized by the low defect formation energy of this facet. This behaviour suggests that surface properties (termination, stepped surface) may have a strong effect on the reactivity. While the reduction of the support accompanies the reaction, its extent does not directly correlate with activity, highlighting the importance of other properties, such as the dissociative adsorption of water and/or CO_2/H_2 desorption. The results of our facet-dependent study are consistent with a redox mechanism, as underlined by $H_2^{18}O$ isotopic exchange experiments demonstrating the ready exchange of surface oxygen.
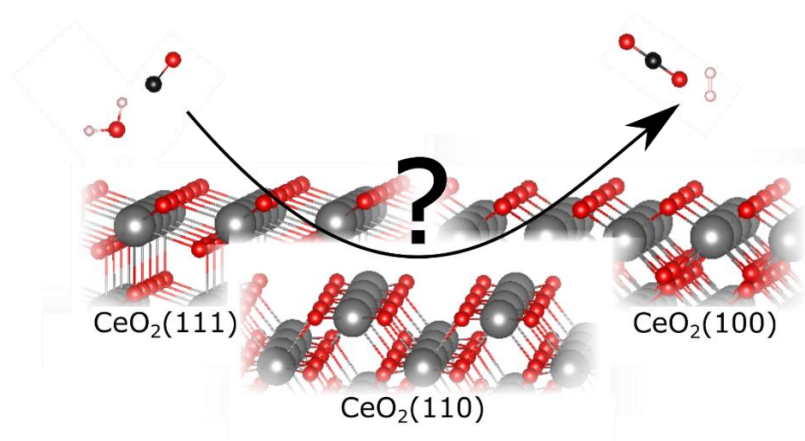
Introduction

Supported-metal (Au, Pt) ceria-based catalysts have been considered as promising candidates for the low-temperature water–gas shift (LT-WGS) reaction,[1–4] which is important for steam reforming to increase the amount of hydrogen and reduce that of carbon monoxide.[5] Furthermore, this reaction is of practical importance in fuel cell applications.[6,7] In this context, the influence of the support properties on the reactivity behaviour is of particular interest. Firstly, the choice of the support material leads to differences in the reactivity of the catalyst,[8] and secondly, the surface termination of the support itself influences the reactivity.[9–12] Among the ceria surfaces, the most stable $CeO_2(111)$ facet has been studied, both experimentally and theoretically, as a bare support,[13–15] but also as a gold-loaded sample in the context of LT-WGS.[3] The other two terminations, i.e., $CeO_2(110)$ and $CeO_2(100)$, have been used in just a few studies as a support for Au/CeO_2 catalysts for LT-WGS.[11,12] To this end, it has been reported that ceria polyhedra, which terminate mainly with $CeO_2(111)$ facets, show the lowest activity for LT-WGS reaction, whereas the thermodynamically less stable $CeO_2(110)$ and $CeO_2(100)$ surfaces, which occur on rods and cubes, are more active.[11,12] These differences in reactivity are related to the thermodynamic stability of the various surface terminations and their different defect formation energies. Additionally, gold interacts differently with the individual surface terminations, the interaction with the $CeO_2(100)$ surface being strongest and that with the $CeO_2(111)$ surface weakest, as has been shown in previous theoretical studies.[16–19] Moreover, according to experimental studies using X-ray photoelectron spectroscopy (XPS) or environmental transmission electron microscopy (ETEM), the interaction at the interface is different for the individual facets, which has been related to the observed catalytic activity.[11,20] Despite these studies, and growing interest in the shape effect on catalytic reactions,[11,21–24] the detailed impact of the surface termination on the reactivity behaviour of Au/CeO_2 catalysts is not well understood and is a topic of current research.[9]

Regarding the mechanism of the LT-WGS reaction, two mechanisms have been proposed in the literature, which are referred to as the redox and associative mechanisms.[1,25,26] In both mechanisms, the cleavage of O–H bonds has been considered to be a key step, but direct experimental evidence for the different ceria facets is scarce.[3] There are several theoretical studies that consider the interaction of water with various ceria surface terminations.[27–29] According to these studies, the interaction of water is lowest on the $CeO_2(111)$ surface and strongest on the $CeO_2(100)$ surface.[27–29] Besides water, also CO was reported to interact differently with the individual facets, which may influence the catalytic activity.[30–32] In fact,

the $CeO_2(110)$ or $CeO_2(100)$ surfaces tend to form strongly adsorbed carbonates on the surface, which may block active sites for the WGS reaction.[30,31,33]

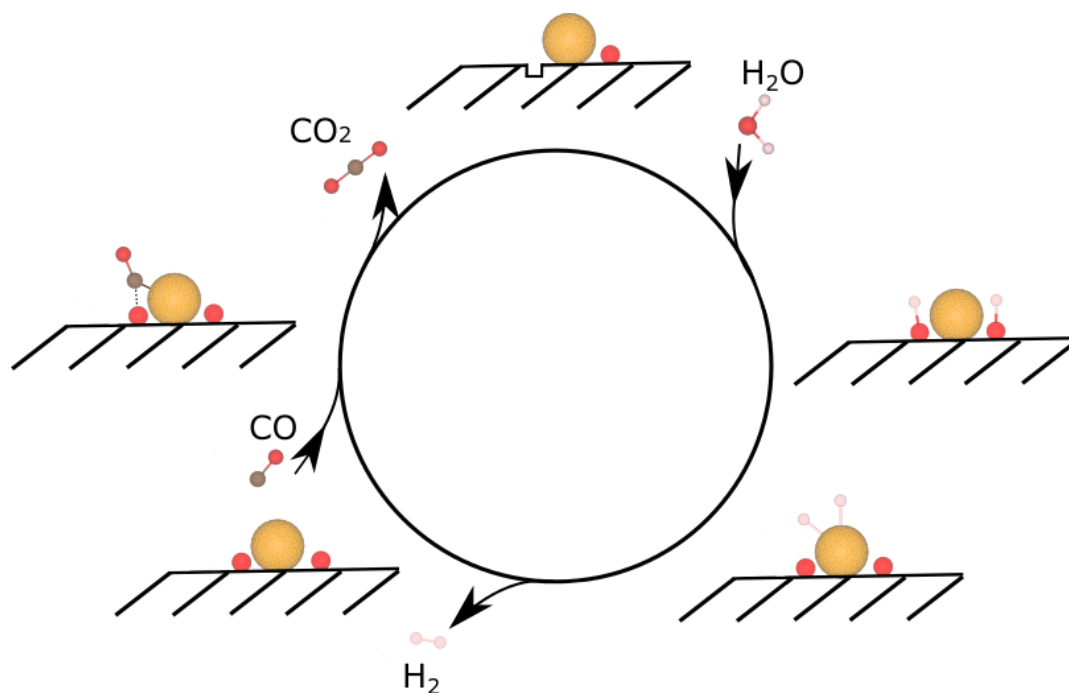**Figure 1:** Proposed mechanism for the WGS reaction over Au/CeO_2 catalysts. For details see text.

In a previous publication, our group reported on the role of surface and bulk oxygen involved in the LT-WGS reaction over gold catalysts supported on polycrystalline ceria, which exposes exclusively the $CeO_2(111)$ surface.[3] Our results are consistent with a redox mechanism, which has been previously proposed[1,34] and discussed[35]. According to this mechanism (see Figure 1), CO is adsorbed at gold sites and reacts with lattice oxygen of the ceria support to produce CO_2 accompanied by the formation of an oxygen vacancy, i.e., the reduction of ceria. Subsequently, water dissociatively adsorbs onto this vacancy, leading to the formation of a hydroxide at the defect itself and a second hydroxide from the reaction of the hydrogen atom with surface oxygen near the defect. Finally, hydrogen from the hydroxides is transferred to the gold particle and recombines to molecular hydrogen. While this mechanism has been discussed in the context of catalysts based on polycrystalline ceria, for a detailed understanding, the influence of the ceria termination should also be considered. For example, the reaction of CO with lattice oxygen requires an energy barrier to be overcome, which is expected to be different for each surface termination because of the different defect formation energies. Besides, as

mentioned above, CO and H_2O interact differently with the individual facets, which may lead to differences in the activity behaviour.

In this contribution, new results on the effect of ceria faceting [(110), (100)] on the WGS reaction mechanism of Au/CeO_2 catalysts will be presented and discussed in the context of previous results on $CeO_2(111)$. We will focus in particular on the oxygen dynamics by using *operando* Raman and UV-Vis spectroscopy, combined with isotope exchange experiments and supported by DFT+U (density functional theory plus Hubbard correction) calculations.

Experimental Section

Catalyst Preparation. $CeO_2(111)$ was prepared by decomposition of $Ce(NO_3)_3 \cdot 6H_2O$ (Alfa Aesar, 99.5%) at 600°C (6 °C/min) for 12 h. After cooling to room temperature the powder was sieved (200 μm) and calcined again using the same protocol.[36,37]

The $CeO_2[(110)+(100)]$ rods and $CeO_2(100)$ cubes were prepared by hydrothermal synthesis of $CeCl_3 \cdot 7H_2O$ (Alfa Aesar, 99%) and $Ce(NO_3)_3 \cdot 6H_2O$ (Alfa Aesar, 99.5%) in a NaOH solution (98%, Grüssing GmbH). The concentration of the NaOH solution in water (electrical conductivity < 3 μS m^{-1}) was 9 M and 6 M for the rods and cubes, respectively.[38,39] For both samples, 79 mL of the NaOH solution was added to 11 mL of precursor solution and stirred for 30 min. Then the solution was transferred to a PTFE (polytetrafluoroethylene, Teflon) autoclave with a volume of about 140 mL and thermally treated in an oven. After being heated to the final temperature at a rate of 1 °C/min, the rods were treated at 140 °C for 48 h and the cubes at 180 °C for 18 h. After cooling to room temperature, the resulting CeO_2 was centrifuged off, washed three times with deionized water, and dried at 85 °C for at least 24 h.

Gold was deposited onto CeO_2 via deposition precipitation,[40] using a 10^{-3} M $HAuCl_4 \cdot 3H_2O$ solution (Carl Roth, 99.9% (rods, cubes); Sigma Aldrich, 99.99% (sheets)) to yield total loadings of 0.5 wt% Au. The rods with 0.5 wt% Au (XPS) were obtained by loading the rods with 0.3 wt% Au (XPS) again. First, the ceria samples were dispersed in a ratio of 1:150 in deionized water, and the pH adjusted to 9 using a 0.1 M NaOH solution (98%, Grüssing GmbH). Subsequently, the chloroauric acid solution was set to pH 9 and added to the ceria dispersion to obtain the desired loading. After the addition, the pH value was checked again and adjusted to the pH value of 9 if necessary. Then, the reaction mixture was heated at 65 °C for 2 h and placed in an ultrasonic bath for 30 min after cooling. Finally, the residue was centrifuged, washed four times with deionized water, and dried at 85 °C for at least 24 h. The sheets were washed with a 0.25% ammonia solution before being washed with water.

Catalyst Characterization. To determine the amount of gold, the catalysts were characterized by XPS on an SSX 100 ESCA spectrometer (Surface Science Laboratories Inc.). In this paper, the amount of gold is given in wt% at the surface, based on the results of the XPS analysis. Briefly, the X-radiation was generated by an Al Kα monochromatic source (9 kV, 10 mA). The sample holder and the analyser were aligned at an angle of 55° to the horizontal. The X-ray beam had an angle of 35° with respect to the analyser horizontal and the sample was rotated by 16° with respect to the X-ray beam. The resolution of the XP spectrometer was 0.054 eV.

To ensure the comparability of the spectra, the u"-signal of Ce(3d) was shifted to the literature value of 916.7 eV for all spectra.[41] The spectra were deconvoluted by Gaussian–Lorentz functions with a 30/70 ratio, whereby the background was subtracted according to Shirley.[42] For further details regarding the XP analysis, please refer to previous studies.[43] Contaminations caused by the synthesis, e.g. chlorine or nitrogen, can be excluded within the sensitivity of the XPS measurements.

Based on N_2 adsorption isotherms at 77 K and application of the BET (Brunauer–Emmett–Teller) model, the specific surface areas were determined to be 61 m²/g for the sheets, 32 m²/g for the cubes, and 88 m²/g for the rods.

The samples were also characterized by transmission electron microscopy (TEM; JEOL JEM-2100F, Tokyo, Japan) to determine the surface termination and to check for potential changes of the surface termination induced by the WGS reaction. The microscope was equipped with a Schottky field emitter and operated at a nominal acceleration voltage of 200 kV. Sample preparation included dispersion in ethanol by means of an ultrasonic bath for 30 s, and placing a few drops on a carbon grid (Plano). After drying, the grid was coated with carbon (Bal-Tec MED010), preventing charging by the electron beam. Based on the TEM experiments, reaction-induced changes of the surface termination can be excluded. TEM images of the bare rods and cubes are shown in Figure S1 of the Supporting information. For the sheets, please refer to our previous work.[44,45] TEM analysis confirms that the morphology and size of the particles does not change during the gold loading and exposure to reaction conditions (not shown).

Operando Characterization*.* For the *operando* measurements, about 20–25 mg of the sample was placed in a stainless-steel sample holder (diameter: 8 mm; depth: 0.5 mm). Details of the setup have been described previously.[36] Briefly, Raman spectra were recorded on a HL5R transmission spectrometer (Kaiser Optical) employing a frequency-doubled Nd:YAG laser (Cobolt) for excitation at 532 nm. The spectral resolution was specified as 5 cm^{-1} and the stability of the band positions was better than 0.3 cm^{-1}. The laser power at the position of the sample was set to a low value of 1 mW to prevent laser-induced changes. Cubes and sheets

were measured by using an exposure time of 80 s and 5 accumulations, whereas for rods an exposure time of 250 s and 2 accumulations were used.

For all measurements an auto new dark and a cosmic ray filter was used. This means that, before each measurement, the background was recorded twice with a closed shutter to determine the background intensity. Furthermore, in each measurement, a second spectrum was recorded to allow for elimination of spikes caused by cosmic rays. As a result, the total measuring time amounted to about 1600 s for cubes and sheets, and about 2000 s for rods. All Raman spectra reported in this work were normalized to the highest intensity band, i.e., the F_{2g} band. Given F_{2g} positions were determined by curve fitting using Lorentz functions.

The UV-Vis measurements were taken in diffuse reflection employing an AvaSpec ULS2048 spectrometer (Avantes), equipped with D_2 and halogen discharge lamps. The measuring time was 60 s, which is composed of an exposure time of 300 ms and 200 averages. Magnesium oxide powder (MgO, Sigma Aldrich), which shows no absorption between 170 and 1100 nm, was used as the white standard.

The sample temperature was determined by means of a Ni / Cr-Ni thermocouple (type K), which is located at the sample holder close to the sample. Sample temperatures deviated by a maximum of 2 °C from the set temperatures.

The gases CO (99.997%, Air Liquide) and argon (99.996%, Westfalen) were dosed by digital mass flow controllers (MFCs, Bronkhorst). The dosage of $H_2^{16}O$ (electrical conductivity <3 μS m^{-1}), $H_2^{18}O$ (97% + ^{18}O, Eurisotop), and $D_2^{16}O$ (99.9% D, Sigma Aldrich) was realized by a controlled evaporator mixer (CEM, Bronkhorst), and a liquid mass flow meter (LFM, Bronkhorst). In all experiments, the total flow rate was 100 mL/min. For quantitative analysis of the gas-phase composition, a FTIR spectrometer (Tensor 20, Bruker) was installed at the outlet of the cell. The spectral resolution was 4 cm^{-1}. The sampling time was set to 1 min, corresponding to the accumulation of 125 spectra. Using calibration curves, the concentrations of CO, $H_2^{16}O$, and CO_2 can be calculated. The catalytic activity is obtained by the quotient of the CO_2 and CO concentration in vol.%. Because H_2 evolution is not accessible by FTIR, we examined the reactivity behaviour of the 0.6 wt% Au/CeO$_2$ sheets in a quartz reactor and an online mass spectrometer to detect H_2.[3] Based on these measurements, the evolution of H_2 is identical to that of CO_2.

DFT Calculations. To facilitate the assignment of vibrational bands, calculations on differently oriented ceria surfaces were performed using DFT+U (PBE+U/4.5 eV), as described in detail in a previous study.[46] All calculations were performed using the Vienna Ab initio Simulation Package (VASP, Version 5.3.5, https://www.vasp.at/), which includes the use of the

GGA(PBE)+U approach (where GGA is the generalized gradient approximation to the exchange-correlation functional), with a parameterization by Perdew, Burke and Ernzerhof (PBE),[47] and a U_{eff} parameter of 4.5 eV for the Ce 4f orbital (PBE+U / 4.5 eV). Only valence electrons with a plane wave cutoff of 400 eV were considered. The Kohn–Sham equations were solved using the projector-augmented wave (PAW) method. Total energies and forces were calculated with a precision of 10^{-6} eV and 10^{-2} eV/Å for electronic and force convergence, respectively. After having allowed for lattice relaxation, a normal mode analysis was performed, followed by the calculation of the Raman intensities of the vibrational modes using density functional perturbation theory (DFPT). For more detailed information please refer to our previous study[46] and to the Supporting Information.

Results

Catalytic Activity. Figure 2 depicts the steady-state catalytic activity during the LT-WGS reaction over gold-loaded ceria sheets, cubes, and rods upon exposure to a stream of $H_2O/CO/Ar$ (8 % H_2O, 2 % CO, Ar; 100 mL/min) at temperatures of 120 °C for sheets and 134 °C for all other samples. When applying identical conditions and the same measurement procedure the unloaded samples show no catalytic activity. As can be seen in Figure 2, the sheets exhibit the highest activity and the cubes have a lower activity, despite the same amount of gold, followed by the rods, giving a first indication of the importance of the support properties, and more specifically, of the surface termination. Interestingly, the rods with the higher gold content (0.5 wt% Au) exhibit the lowest activity of all samples, illustrating the importance of the interaction between support and gold for the catalytic activity, whereby the size of the gold particles is proposed to play a crucial role.[48] The fact that the sheets show the highest activity appears to contradict the expectations of a defined $CeO_2(111)$ terminating surface.[11,12] However, previous TEM images of our polycrystalline ceria sample have shown the presence of stepped facets.[44,45] Note that this sample was also used for the present work. These stepped sites may have a positive effect on activity during CO oxidation,[45] because of the changing surface properties, such as interactions with deposited gold, which in turn may result in different interactions with gas-phase molecules, or changes in the defect formation energy.[49–51] To gain more detailed insight into the mechanism of the LT-WGS reaction over Au/CeO_2 catalysts, *operando* Raman and UV-Vis spectroscopy in combination with isotope exchange experiments was applied, as discussed in the following.
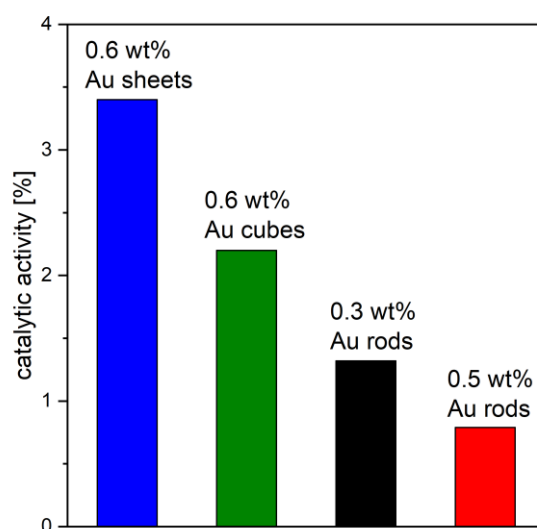
Figure 2: Catalytic activity during LT-WGS reaction over 0.6 wt% Au/CeO$_2$ sheets (blue), 0.6 wt% Au/CeO$_2$ cubes (green), 0.3 wt% Au/CeO$_2$ rods (black), and 0.5 wt% Au/CeO$_2$ rods (red) upon exposure to a stream of H$_2$O/CO/Ar (8 % H$_2$O, 2 % CO, Ar; 100 mL/min) at 120 °C for the sheets and at 134 °C for all other samples. The catalytic activity was measured after at least 1 h on stream.

***Operando* UV-Vis Spectroscopy.** Figure 3 depicts *operando* UV-Vis spectra of the Au/CeO$_2$ catalysts (solid lines) in comparison to spectra recorded in Ar flow (dashed lines). The UV-Vis spectra of the gold-loaded samples in Ar show absorption between 450 nm and 900 nm, in contrast to the bare ceria samples (see Figure S2 in Supporting Information). It is noticeable that the sheets have the highest absorption and, despite a similar amount of gold, the absorption of the rods and cubes is lower. The absorption of the rods exhibits a strong dependence on the gold content. In fact, the rods loaded with 0.3 wt% Au show hardly any increase in absorption in comparison to the bare rods. Furthermore, upon closer inspection, differences in the profile of this band can be observed, i.e., the band of the rods and cubes is significantly broader than that of the sheets. From these observations it can be concluded that the band is related to the gold loading, but that the amount of gold is not the only factor that has an influence. For this reason, given that the gold surface plasmons in this region originate from the presence of metallic gold, it can be said that the observed absorption is attributable to the fraction of metallic gold,[52,53] which can be confirmed by XPS measurements. In fact, in our previous study, the Au 4f photoemission showed a fraction of metallic Au of 70 % for the Au-loaded sheets.[3] For

all other samples, smaller Au^0 contributions are observed (see Figures S3 and S4 in Supporting Information): a Au^0 fraction of 40 % for the Au-loaded cubes, 63 % for the 0.3 wt% Au rods, and 57 % for the 0.5 wt% Au rods.
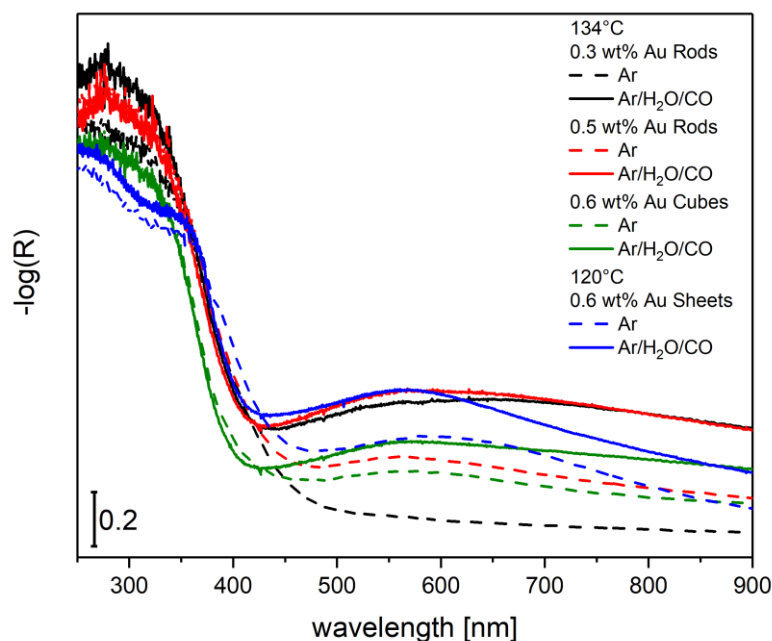

Figure 3: *Operando* UV-Vis reflectance spectra of the Au/CeO_2 catalysts (solid lines) in comparison to spectra obtained under a stream of Ar prior to reaction (dashed lines). Reaction conditions consist of a feed of 8% H_2O/2% CO/Ar at a total flow of 100 mL/min, and a temperature of 120 °C for the sheets and 134 °C for all other samples. Spectra correspond to 0.6 wt% Au/CeO_2 sheets (blue), 0.6 wt% Au/CeO_2 cubes (green), 0.3 wt% Au/CeO_2 rods (black), and 0.5 wt% Au/CeO_2 rods (red).

Switching from Ar to reaction conditions leads to a strong increase in absorption between 450 nm and 900 nm for all catalyst samples. The largest increase is observed for the rods loaded with 0.3 wt% Au, followed by the rods with 0.5 wt% Au loading. This behaviour can be explained by the easier reducibility of the rods, as they contain the CeO_2(110) facet, which has the lowest defect formation energy.[54] The reduction leads to a charge transfer from Ce^{3+} to Ce^{4+}, which gives rise to absorption at around 570 nm.[55] In previous studies, such an increase in absorption has also been observed on bare ceria samples in the presence of hydrogen at elevated temperatures (200–700 °C).[41,56] Summarizing, the absorption in the range between 450 nm and 900 nm originates from gold surface plasmons and a charge transfer between Ce^{3+} and Ce^{4+}.

UV-Vis spectra recorded in a stream of H_2O/Ar after exposure to reaction conditions show a decrease in the absorption in the range 450–900 nm (see Figure S5 in Supporting Information), but the initial state in Ar is not reached again, neither in H_2O/Ar nor by cooling the sample under Ar atmosphere. The observed behaviour indicates an agglomeration of the gold particles, leading to an enrichment of neutral gold, as has also been shown in earlier studies.[53,57–59]

***Operando* Raman Spectroscopy.** To gain insight into the structural dynamics of the catalysts and the presence of adsorbates, Raman spectroscopy was applied. Figure 4A shows *operando* Raman spectra, obtained with 532 nm wavelength excitation, of the facet-dependent Au/CeO_2 catalysts under reaction conditions (2% CO/8% H_2O/Ar). The spectra are dominated by the F_{2g} band at around 450 cm^{-1}, which has been cut off to give an enlarged view of the other features. Please note that the F_{2g} band positions are given at the top right of the figure. As a reference, the spectra for the bare ceria samples are shown in the Supporting Information (see Figure S6) with F_{2g} bands located at 451.3, 458.1, and 461.7 cm^{-1} for the rods, cubes, and sheets, respectively, and defect bands located within the 540–590 cm^{-1} range.

Owing to the presence of gold-induced fluorescence, the comparison of relative Raman intensities needs to be done with care. In contrast to the cubes and rods with 0.5 wt% Au, for the rods with 0.3 wt% Au and the sheets only a small background is observed. In this case, we consider a comparison of the defect-related bands acceptable. In this context the Au-loaded rods show more intense defect bands at 540 cm^{-1} and 590 cm^{-1}. Besides, it is noticeable that the F_{2g} band of the Au-loaded rods is located at 448.5 cm^{-1} and that of the Au-loaded sheets at 456.4 cm^{-1}. Note that the F_{2g} red-shifts, that occur under reaction conditions, originate from an expansion of the unit cell on the basis of the greater ionic radius of the Ce^{3+} formed upon ceria reduction and can be related to the number of oxygen vacancies in ceria, as discussed previously.[60] These two observations clearly indicate a greater extent of reduction of the Au-loaded rods.
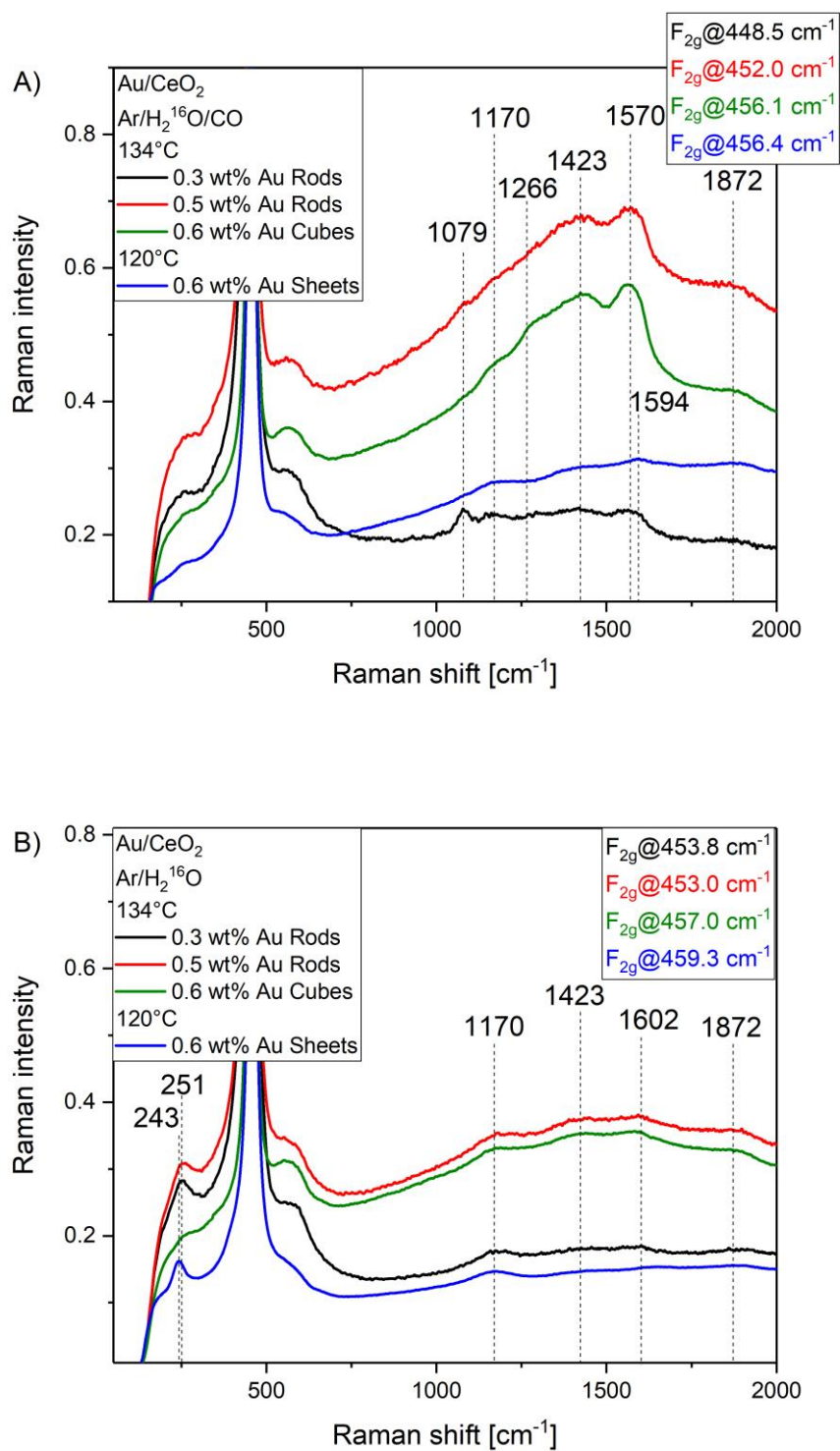
Figure 4: A) *Operando* Raman spectra of the Au/CeO₂ catalysts recorded under reaction conditions (2% CO/8% H₂O/Ar). **B)** *In situ* Raman spectra recorded in 8% H₂O/Ar after reaction. The total flow rate is 100 mL/min. The temperature is 120 °C for the sheets and 134 °C for all other samples. The F$_{2g}$ bands have been cut off for clarity; the F$_{2g}$ band positions are given at the top right. Spectra correspond to 0.6 wt% Au/CeO₂ sheets (blue), 0.6 wt% Au/CeO₂

cubes (green), 0.3 wt% Au/CeO$_2$ rods (black), and 0.5 wt% Au/CeO$_2$ rods (red). Spectra were recorded at 532 nm excitation.

In the region of oxygen adsorbates, a Raman band is observed at 1079 cm^{-1} in the case of the Au-loaded rods, which is hardly or not at all detected for the other samples. Interestingly, this band can only be observed under reaction conditions and is much more intense for the 0.3 wt% Au sample. Additionally, a band at around 1266 cm^{-1} is detected for the Au-loaded cubes, whereas bands at 1423 cm^{-1} and 1570 cm^{-1} were observed for Au-loaded cubes and rods. The band at around 1594 cm^{-1} originates from a formate species adsorbed at the CeO$_2$(111) facet,[3] whereas the weak band at around 1872 cm^{-1} can be assigned to molecular water. To explore the nature of the unassigned bands, including the feature at 1079 cm^{-1}, we performed isotope exchange experiments combined with DFT calculations, as will be discussed below.

Figure 4B shows *in situ* Raman spectra of the Au/CeO$_2$ catalysts, recorded in 8% H$_2$O/Ar atmosphere after reaction. A comparison of the spectra under reaction conditions (see Figure 4A) with those taken after reaction (H$_2$O/Ar) shows that the 2TA overtone at 251 cm^{-1} almost completely disappears under reaction conditions and reappears in H$_2$O/Ar. Besides, the 2LO-overtone at 1170 cm^{-1} is more pronounced in H$_2$O/Ar atmosphere. This behaviour may originate from the strong change of the electronic structure under reaction conditions (see Figure 3), leading to a decrease in intensity and signal-to-noise ratio. Note that the Au-loaded sheets show an additional band in the region of the 2TA overtone at 243 cm^{-1}, which is attributed to the longitudinal mode of surface oxygen, as previously discussed.[46] The loss of intensity of this band under reaction conditions can be explained by the reaction or removal of surface oxygen. The regeneration of defects is consistent with a blue-shift of the F$_{2g}$ band of 2.9 cm^{-1} when switching from reaction conditions to H$_2$O/Ar atmosphere. Such a regeneration is observed for all samples and is most pronounced for the rods with 0.3 wt% Au loading, as reflected in a 5.8 cm^{-1} shift of the F$_{2g}$ band. For the other two samples, the blue-shift is less pronounced, and amounts to about 1 cm^{-1}.

Under H$_2$O/Ar atmosphere, the band at 1423 cm^{-1} becomes more prominent for the Au-loaded cubes and rods with 0.5 wt% Au loading. Furthermore, the broad band at 1570 cm^{-1} disappears, and a small feature at 1602 cm^{-1} is detected. Note that owing to the width of the 1570 cm^{-1} band we cannot exclude the presence of the 1602 cm^{-1} feature under reaction conditions.

In summary, the Raman data demonstrates a significant difference in the reducibility of the samples and their interactions with molecules from the gas phase. As a prominent example of facet-dependent adsorption behaviour, the Au-loaded rods show a band at 1079 cm^{-1} under reaction conditions.
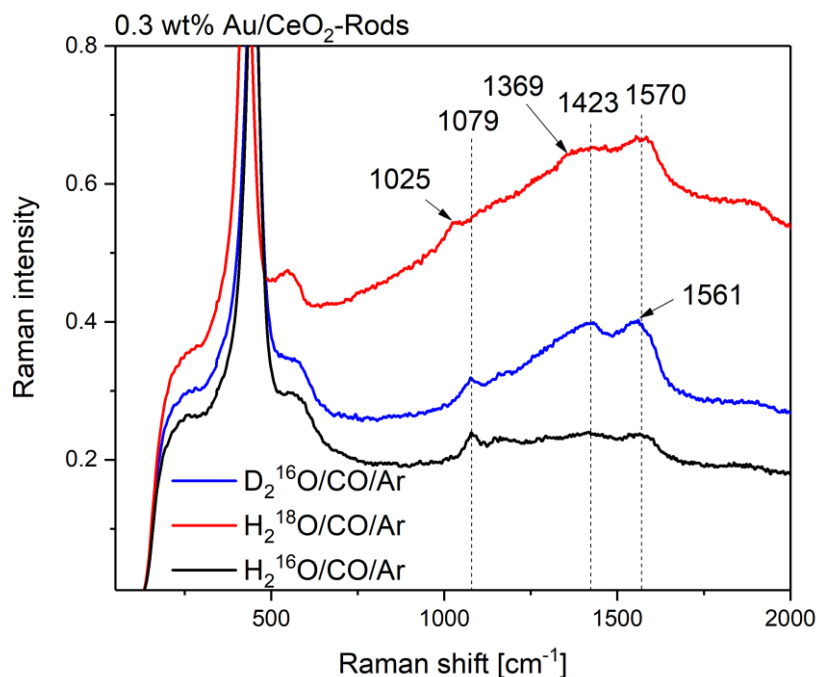

Figure 5: *Operando* Raman spectra of the 0.3 wt% Au/CeO$_2$ rods. Obtained under reaction conditions (2% CO/ 8% H$_2$O/Ar) at 134 °C and at a total flow rate of 10 mL/min using the water isotopes D$_2$^{16}O (blue), H$_2$^{18}O (red), and H$_2$^{16}O (black). Raman spectra were recorded at 532 nm excitation.

Isotope exchange experiments. To explore the nature of the observed bands, isotope exchange experiments were performed using H$_2$^{18}O and D$_2$^{16}O. Figure 5 depicts the *operando* Raman spectra of the 0.3 wt% Au/CeO$_2$ rods under reaction conditions. As discussed in the following, several isotope shifts were observed. The use of H$_2$^{18}O leads to a red-shift of the band located at 1079 cm^{-1} to 1025 cm^{-1}, which is not observed for D$_2$^{16}O. This clearly shows that this vibrational mode involves oxygen but not hydrogen. Considering the spectral region, the presence of several vibrations related to carbonate and molecular oxygen adsorbates may be feasible. To facilitate the band assignment, DFT calculations were performed (see Figure S7 and Table S1), which help to readily exclude Raman active carbonate stretching vibrations (ν_{CO_3}) due to their mostly excessive shifts (based on the harmonic approximation). On the other

hand, the observed behaviour would be consistent with the O-O stretching vibration of a superoxide. In fact, DFT calculations (see Figure S8 and Table S2) support the assignment of the 1079 cm^{-1} band to superoxide adsorbed on a CeO_2(110) facet, which occurs at significantly lower wavenumber than on the previously studied CeO_2(111) or CeO_2(100) facets.[61] Due to the exclusive occurrence of the 1079 cm^{-1} band under reaction conditions, which have been shown to lead to ceria reduction (see Figure 4A), we can attribute the Raman band at 1079 cm^{-1} to superoxide adsorbed on a reduced CeO_2(110) surface.

As can be seen in Figure 5, the use of $H_2^{18}O$ induces a red-shift of the band at 1423 cm^{-1} to 1369 cm^{-1}. The same behaviour is also observed in the case of the Au-loaded cubes (not shown). These bands may be assigned to vibrations of carbonate species on CeO_2(100) based on DFT calculations and the lack of an isotope shift when D_2O is used.[62] Upon exposure to $D_2^{16}O$, the band at 1570 cm^{-1} shows a slight shift to 1561 cm^{-1}. Based on the position and observed isotope exchange behaviour, this feature is assigned to a formate species. In this context it is worth mentioning that, according to previous DFT calculations, replacing the lattice oxygen by ^{18}O has no influence on the OCO vibrations.[3]

Dynamical behaviour under WGS reaction conditions. In the following, the dynamical behaviour of the facet-dependent Au/CeO$_2$ catalysts will be discussed by relating the catalytic activity to the spectroscopic changes (see Figure 6). As spectroscopic properties the shift of the F_{2g} position (from Raman spectra) and the change in absorbance at 570 nm (from UV-Vis spectra) will be considered. In the course of the experiments, the catalysts were first exposed to Ar before the switch to reaction conditions (2% CO/8% H_2O/Ar) occurred, followed by exposure to 8% H_2O/Ar, and a final cooling phase to 48 °C in Ar. In general, all samples show the same trends in the variation of the absorption and the F_{2g} shift. Regarding the absorption behaviour, a strong increase upon exposure to reaction conditions and a smaller decrease when switching to 8% H_2O/Ar atmosphere is observed, but none of the samples returns to its initial state. Among the Au/CeO$_2$ samples, the Au-loaded rods show the biggest and the Au-loaded cubes the smallest change in absorption when the feed is switched from Ar to reaction conditions. For comparison, for the unloaded samples, only very small or no changes were observed in this spectral range. Changes in absorption are related to gold surface plasmons and a reduction of the support, leading to Ce^{3+}–Ce^{4+} transitions. When comparing the absolute absorption changes with the activity of the Au/CeO$_2$ catalysts, no correlation is recognizable at this point. Anyway, the activity is related to an increase in absorption, but the extent of the

absolute change does not play a crucial role for the catalytic activity. These observations related to the activity indicate that reducibility alone is not decisive for the activity. This is apparent from a comparison of activity data in Figure 2 and the absolute changes of the F_{2g} position and the absorption at 570 nm in Figure 6. In the following, the oxygen dynamics of the bare samples are discussed, which further emphasizes the last statement.
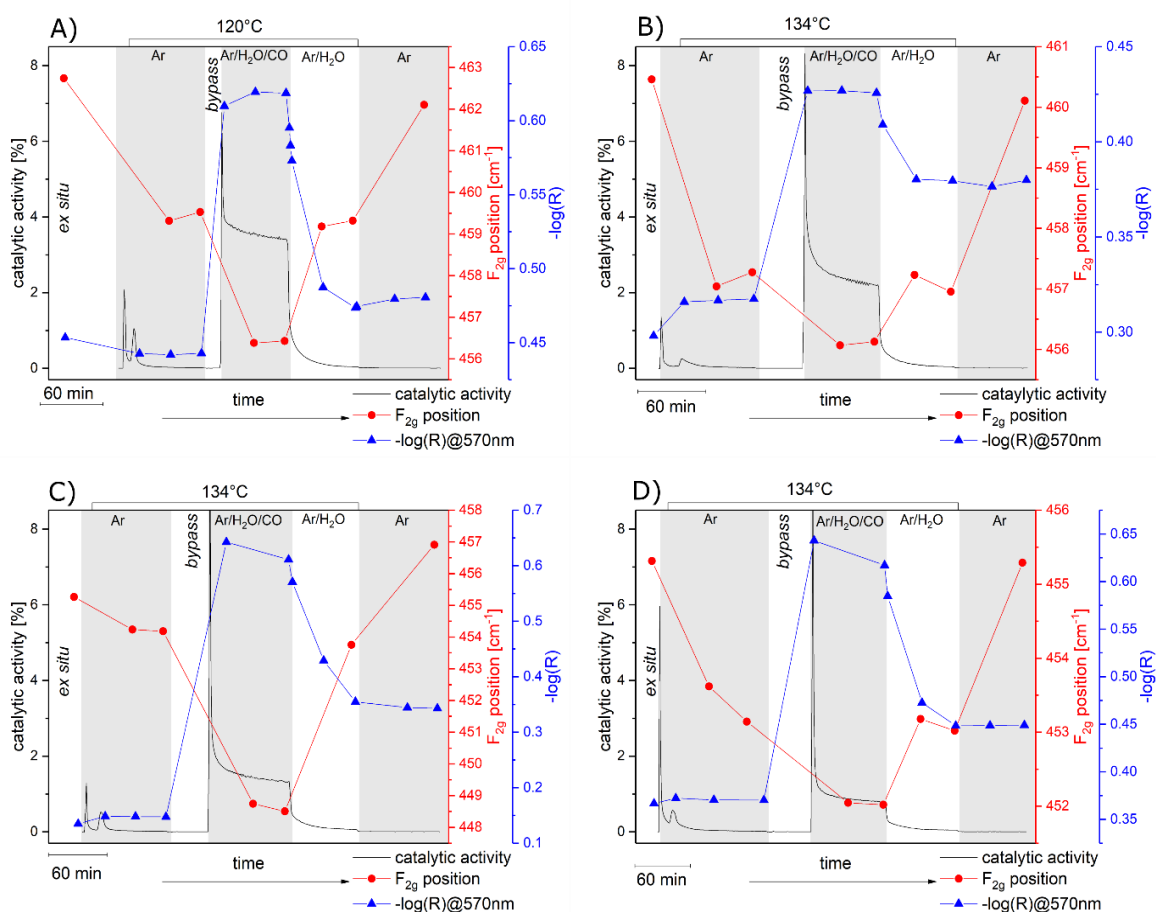

Figure 6: *Operando* Raman (red) and UV-Vis (blue) results shown together with the catalytic activity (black) of **A)** 0.6 wt% Au/CeO$_2$ sheets, **B)** 0.6 wt% Au/CeO$_2$ cubes, **C)** 0.3 wt% Au/CeO$_2$ rods, and **D)** 0.5 wt% Au/CeO$_2$ rods at 120 °C (sheets) or 134 °C (cubes, rods) during WGS reaction (2% CO/8% H$_2$O/Ar) at a total flow rate of 100 mL/min. Raman spectra were recorded at 532 nm wavelength excitation. Prior to reaction the catalyst was exposed to Ar; after reaction the catalyst was exposed to Ar/H$_2$O (8% H$_2$O) and then cooled to 48 °C in Ar.

To this end details of the subsurface oxygen dynamics, as measured by the F_{2g} band position, are depicted in Figure 7 following the experimental protocol discussed above (see Figure 6), including a comparison of loaded with unloaded ceria samples. Furthermore, the F_{2g}

16

band positions recorded during $H_2^{18}O$ exposure are shown. As a result of oxygen isotope exchange, large amounts of ^{18}O are detected in the ceria subsurface, indicating the facile dissociation of water at the catalyst surface and subsequent oxygen transfer from the surface to deeper layers. Interestingly, this behaviour is facet dependent, with $CeO_2[(110)+(100)]$ rods showing the strongest dynamics, which is also present in the absence of gold. In contrast, in the case of $CeO_2(111)$ facets, gold is required to induce a substitution of lattice oxygen.

Upon closer inspection, further differences between the samples can be seen, as discussed in the following. As shown in Figure 7A, the bare sheets undergo only small changes, in contrast to the dynamics exhibited by the Au-loaded sheets. Thus, it appears that the gold loading significantly reduces the defect formation energy, so that an increase in temperature is sufficient to reduce the material. The largest change in F_{2g} position within the sequence of steps is observed under reaction conditions, and if $H_2^{18}O$ is employed, a further F_{2g} red-shift occurs, originating from the replacement of lattice oxygen by ^{18}O. This latter (isotope-induced) red-shift is 16 cm^{-1}, in comparison to the calculated F_{2g} shift of 24 cm^{-1} for complete substitution.[3] When CO is switched off, the catalyst regenerates, as indicated by a slight blue-shift of the F_{2g} band. If the feed is switched to pure Ar and the sample cooled down, the F_{2g} position returns to its initial value for both water isotopes, which can be explained by the dilution of subsurface ^{18}O by ^{16}O from the bulk in the absence of $H_2^{18}O$, as discussed previously.[3]

For the cubes, lower initial F_{2g} positions are observed, indicating a higher oxygen defect concentration. This can be rationalized by the lower defect formation energy of the $CeO_2(100)$ facet compared to the $CeO_2(111)$ facet. During the treatments the bare cubes show small F_{2g} shifts, which are attributed to temperature-related mode softening.[63,64] In the presence of gold the extent of the F_{2g} shifts slightly increases, as a result of an easier reduction of the material due to a decrease in defect formation energy.[65] Unlike the sheets, the bare cubes show a further red-shift of the F_{2g} band after reaction conditions when $H_2^{18}O$ is used, indicating that an exchange of lattice oxygen can take place in the absence of any catalytic activity. The fact that a further exchange of oxygen is observed upon exposure to $H_2^{18}O$/Ar suggests that water adsorbs more extensively in the absence of CO in the feed (thus avoiding other adsorbates). In contrast, for the $CeO_2(111)$ sheets, no such behaviour is detected, owing to the lower interaction of water with the $CeO_2(111)$ surface.[27–29]

In the case of the Au-loaded cubes, a ready exchange of lattice oxygen under reaction conditions is observed, as indicated by the F_{2g} red-shift of 17 cm^{-1}. While the magnitude of the shift is similar to that of the Au-loaded sheets, the behaviour after reaction conditions is different, i.e., the F_{2g} band shows a further red-shift, similar to the bare cubes. Thus, the

exchange of lattice oxygen continues, even without any WGS activity. The maximum of the shift corresponds to 20.5 cm^{-1} and is close to the value for complete substitution of 22.6 cm^{-1}, which we obtained by DFT calculations. When the sample is cooled down in Ar, a blue-shift is observed, but the F_{2g} band does not return to its original position, in contrast to the behaviour observed for the Au-loaded sheets. The observation that in the case of the Au-loaded cubes the initial state is only partially recovered can be explained by an equilibration of subsurface O^{18} with O^{16} from the bulk, which is not completed on the timescale of the experiment. This behaviour is consistent with that of the Au-loaded sheets (see above), considering the different extent of isotope exchange for the cube- and sheet-based samples.

Finally, the subsurface oxygen dynamics of the rods is depicted in Figure 7C, which includes data for both gold loadings as well as the bare rods. Generally, the F_{2g} positions of the rods are significantly lower than those of the cubes and sheets. For the unloaded rods the F_{2g} band is located at 450 cm^{-1}, which corresponds to a red-shift of more than 13 cm^{-1} compared to the sheets. One reason for this behaviour is the easier reducibility of the $CeO_2(100)$ and $CeO_2(110)$ facets of the rods. Interestingly, in the presence of $H_2^{16}O/CO/Ar$, the sample with 0.3 wt% Au shows a distinct shift of 5.7 cm^{-1}, whereas the 0.5 wt% Au sample shows only a minor shift, comparable to that of the bare rods. On switching to $H_2^{16}O/Ar$ and Ar, defect regeneration occurs, as indicated by the F_{2g} band positions resembling the initial values.

In the presence of $H_2^{18}O$, even the unloaded rods show a red-shift of the F_{2g} band that is larger than that of the cubes. Unlike for the gold-loaded samples, the F_{2g} band shifts further to the red when the conditions are switched from reaction to $H_2^{18}O/Ar$ atmosphere. Moreover, cooling in Ar induces only a small recovery, which clearly indicates that the isotope exchange of lattice oxygen penetrates deeper into the subsurface/bulk of rods in comparison to the cubes and sheets. In the case of the gold-loaded samples, very strong red-shifts of 25.1 cm^{-1} and 26.8 cm^{-1} are observed under reaction conditions for the 0.3 wt% Au and 0.5 wt% Au samples, respectively, followed by blue-shifts of 7.6 cm^{-1} and 5.4 cm^{-1} after reaction. This behaviour can be explained by the strongly reduced state of the samples created under reaction conditions, which leads to (at least) partial regeneration after the reaction. It is worth mentioning that the 0.3 wt% Au sample undergoes larger shifts despite its lower WGS activity. This suggests that the amount of gold plays an important role in the exchange of lattice oxygen, but not necessarily with respect to the activity.

In summary, our findings show that for the reducibility behaviour of the samples, as measured by the red-shift of the F_{2g} band upon switching from Ar to reactive atmosphere, the surface termination is not the only decisive factor. This statement is justified by a comparison

of the cubes and sheets (see Table 1), according to which the sheets are subject to larger shifts. As a consequence, the sheets are more strongly reduced than the cubes, despite their $CeO_2(111)$ termination. This behaviour can be rationalized by the initially higher defect concentrations of the cubes, and/or by a lowering of the defect formation energy at stepped surfaces.[49]

Furthermore, by comparing Table 1 with Figure 2, it is also evident that there is no correlation between the extent of the F_{2g} red-shift and the catalytic activity. This is direct proof that the activity depends not only on the defect formation energy but also on other parameters, such as the desorption energy of CO_2 and/or the activation of H_2O. In this context it has previously been shown that the interaction of CO_2 and H_2O with $CeO_2(110)$ and $CeO_2(100)$ facets is stronger than with the $CeO_2(111)$ facet. On one hand, this may lead to an easier activation of the above molecules, but on the other hand, more strongly adsorbed species may be formed, which may have a negative effect on catalytic activity.[27–31] Previous studies reported a lowering of the CO_2 desorption energy at stepped sites by 0.85 eV (comparison between Au/CeO_2[66] and Au/CeO_2-U[49]). Based on the detailed TEM analysis of our $CeO_2(111)$-based Au/CeO_2 catalyst providing clear evidence for the presence of stepped sites,[44] we may therefore attribute the increased WGS activity of the Au-loaded sheets, as compared to the rod- and cube-based catalysts, to these stepped sites.[49]

Table 1: Absolute F_{2g} shifts of the Au-loaded samples when switching from Ar to reaction conditions ($CO/H_2{}^{16}O/Ar$) and from reaction conditions to $H_2{}^{16}O/Ar$. Shifts of the bare ceria samples are always smaller than 0.1 cm^{-1}. The experimental conditions correspond to those in Figure 6.

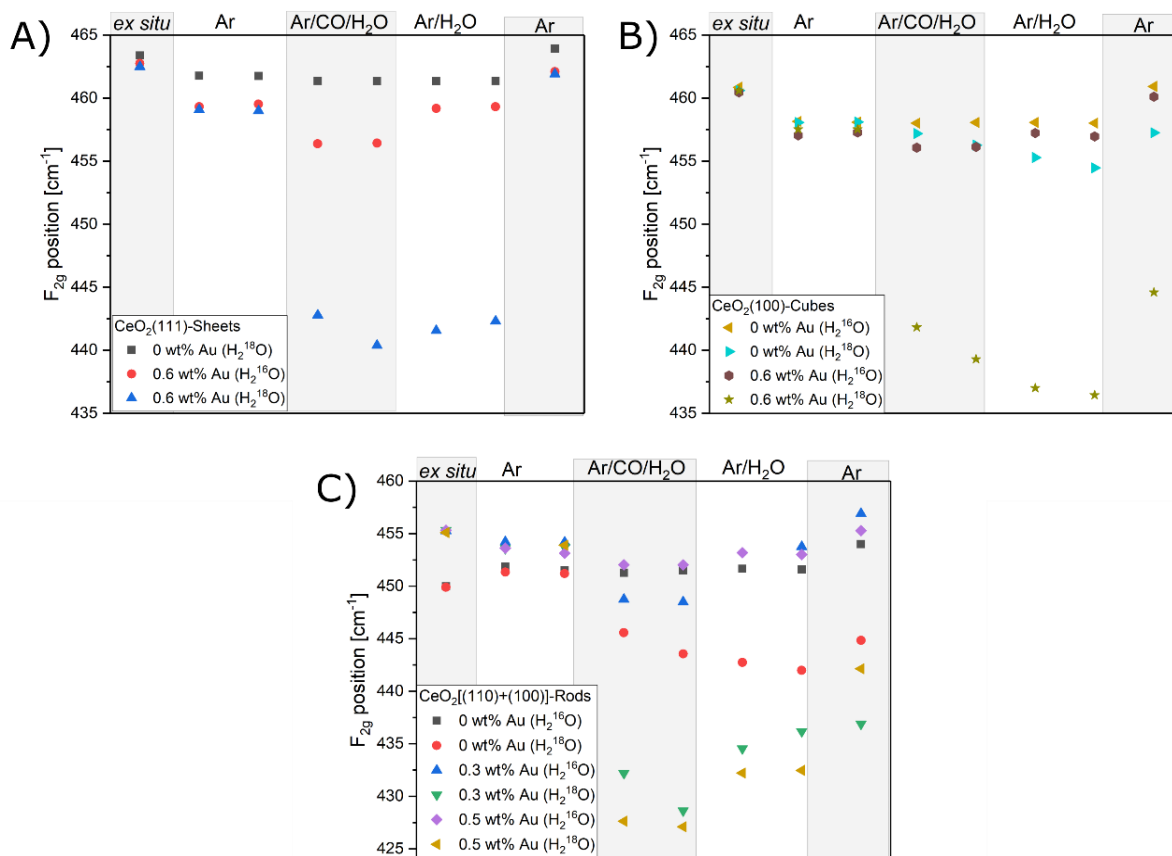| Sample	$\Delta_{(Ar \to CO/H_2O/Ar)}$ [cm^{-1}]	$\Delta_{(CO/H_2O/Ar \to H_2O/Ar)}$ [cm^{-1}]
Au/Sheets	3.1	2.9
Au/Cubes	1.1	0.8
0.3 wt% Au/Rods	5.7	5.3
0.5 wt% Au/Rods	1.1	1.0

Figure 7: Oxygen dynamics based on the Raman F_{2g} position for **A)** 0.6 wt% Au/CeO$_2$ sheets, **B)** 0.6 wt% Au/CeO$_2$ cubes, and **C)** Au/CeO$_2$ rods in comparison to the bare ceria samples. The Au loadings for the rods were 0.3 wt% Au and 0.5 wt% Au; experiments were performed using $H_2{}^{16}O$ and $H_2{}^{18}O$. The experimental conditions correspond to those given in the caption of Figure 6.

Insight into the reaction mechanism. Our findings strongly indicate that beside the amount of gold, support properties such as the type of facets and the presence of steps play an important role regarding the reactivity behaviour of Au/CeO$_2$ catalysts in the WGS reaction. In particular, the defect formation energy alone, which differs for the individual surface terminations, is not decisive for a high activity, and we do not observe a correlation of activity with the number of defects, as proposed in the literature.[67] However, there are other aspects, such as the desorption energy of CO$_2$ and the activation of H$_2$O, that need to be considered. Regarding H$_2$O activation is has been shown for Cu/CeO$_2$ catalysts that water dissociation may be rate-determining for the WGS reaction.[68] According to the literature, the interaction of water on the clean surface is

lowest for $CeO_2(111)$ and strongest for $CeO_2(100)$.[27–29] It should, however, be mentioned that the dissociation of water is more preferred on oxygen vacancies than on the clean surface[69,70] and in the presence of oxygen vacancies the adsorption is weakest for $CeO_2(111)$ and strongest for $CeO_2(100)$.[28] Therefore, it will be important to investigate the interaction of water with different surface terminations in great detail in the future.

Turning now to the proposed mechanism for the WGS reaction (see Figure 1), we see that our spectroscopic findings for Au/CeO_2 catalysts are consistent with a redox mechanism, independent of the surface termination. The isotope exchange experiments also show that the proposed dissociative adsorption of water involves an oxygen vacancy, as evidenced by the regeneration after reaction conditions in a stream of H_2O/Ar and by the replacement of ^{16}O by ^{18}O.

Conclusions

Our results demonstrate the potential of combining *operando* spectroscopies with isotope experiments to monitor the facet-dependent dynamics of different surface and bulk oxygen species in Au/CeO_2 catalysts during WGS conditions. Supported by DFT calculations, new insights into the reaction mechanism were obtained. Under reaction conditions a reduction of the ceria support materials takes place, which also involves subsurface oxygen. While all catalysts show reduction during reaction conditions, there is no correlation of the extent of reduction with the catalytic activity. As a result of the particularly strong reduction of the rods with 0.3 wt% Au loading during WGS reaction, a superoxide band is observed at 1079 cm^{-1}, in agreement with theoretical calculations. The reduction of the Au/CeO_2 samples is also responsible for the ready dissociation of water, a crucial step in the WGS reaction. The observed red-shift of the F_{2g} band and exchange of oxygen using $H_2{}^{18}O$ are consistent with a redox-type mechanism.

We found the WGS reaction to be strongly facet-dependent and to depend not only on the surface termination but also on other factors, such as the presence of stepped sites. In fact, based on our results, gold loaded on a stepped $CeO_2(111)$, as in the case of the sheets, shows the highest WGS activity. The two less-stable surfaces, i.e., $CeO_2(110)$ and $CeO_2(100)$, are able to adsorb CO as carbonate species, which may block active sites and lead to lower CO conversion, as indicated by the presence of carbonate bands at 1423 cm^{-1} in the Raman spectra during reaction conditions (see Figure 4).

Acknowledgements

Supporting Information

Additional information is provided in a separate file.

References

1   Q. Fu, H. Saltsburg and M. Flytzani-Stephanopoulos, *Science (80-.).*, 2003, **301**, 935–938.

2   C. M. Kalamaras, I. D. Gonzalez, R. M. Navarro, J. L. G. Fierro and A. M. Efstathiou, *J. Phys. Chem. C*, 2011, **115**, 11595–11610.

3   C. Schilling and C. Hess, *ACS Catal.*, 2019, **9**, 1159–1171.

4   A. Luengnaruemitchai, S. Osuwan and E. Gulari, *Catal. Commun.*, 2003, **4**, 215–221.

5   C. Ratnasamy and J. P. Wagner, *Catal. Rev.*, 2009, **51**, 325–440.

6   J. M. Zalc and D. G. Löffler, *J. Power Sources*, 2002, **111**, 58–64.

7   D. L. Trimm, *Appl. Catal. A Gen.*, 2005, **296**, 1–11.

8   P. Panagiotopoulou and D. I. Kondarides, *Catal. Today*, 2006, **112**, 49–52.

9   A. Trovarelli and J. Llorca, *ACS Catal.*, 2017, **7**, 4716–4735.

10   T. Montini, M. Melchionna, M. Monai and P. Fornasiero, *Chem. Rev.*, 2016, **116**, 5987–6041.

11   R. Si and M. Flytzani-Stephanopoulos, *Angew. Chemie Int. Ed.*, 2008, **47**, 2884–2887.

12   S. Agarwal, L. Lefferts, B. L. Mojet, D. A. J. M. Ligthart, E. J. M. Hensen, D. R. G. Mitchell, W. J. Erasmus, B. G. Anderson, E. J. Olivier, J. H. Neethling and A. K. Datye, *ChemSusChem*, 2013, **6**, 1898–1906.

13   Z. Wu and S. H. Overbury, *Catalysis by Materials with Well-Defined Structures*, 2015.

14   J. Paier, C. Penschke and J. Sauer, *Chem. Rev.*, 2013, **113**, 3949–3985.

15   M. V. Ganduglia-Pirovano, A. Hofmann and J. Sauer, *Surf. Sci. Rep.*, 2007, **62**, 219–270.

16   A. Chutia, D. J. Willock and C. R. A. Catlow, *Faraday Discuss.*, 2018, **208**, 123–145.

17   K.-J. Zhu, Y.-J. Yang, J.-J. Lang, B.-T. Teng, F.-M. Wu, S.-Y. Du and X.-D. Wen, *Appl. Surf. Sci.*, 2016, **387**, 557–568.

18   C. Zhang, A. Michaelides and S. J. Jenkins, *Phys. Chem. Chem. Phys.*, 2011, **13**, 22–33.

19   M. Nolan, *J. Chem. Phys.*, 2012, **136**, 134703.

20   N. TA, J. LIU (Jimmy) and W. SHEN, *Chinese J. Catal.*, 2013, **34**, 838–850.

21   Z. A. Qiao, Z. Wu and S. Dai, *ChemSusChem*, 2013, **6**, 1821–1833.

22   J. Han, H. J. Kim, S. Yoon and H. Lee, *J. Mol. Catal. A Chem.*, 2011, **335**, 82–88.

23   L. Liu, Z. Yao, Y. Deng, F. Gao, B. Liu and L. Dong, *ChemCatChem*, 2011, **3**, 978–989.

24   Z. Wu, V. Schwartz, M. Li, A. J. Rondinone and S. H. Overbury, *J. Phys. Chem. Lett.*, 2012, **3**, 1517–1522.

25   Y. Chen, J. Cheng, P. Hu and H. Wang, *Surf. Sci.*, 2008, **602**, 2828–2834.

26   S. Aranifard, S. C. Ammal and A. Heyden, *J. Catal.*, 2014, **309**, 314–324.

27   T. Kropp, J. Paier and J. Sauer, *J. Phys. Chem. C*, 2017, **121**, 21571–21578.

28   M. Molinari, S. C. Parker, D. C. Sayle and M. S. Islam, *J. Phys. Chem. C*, 2012, **116**, 7073–7082.

29   D. Fernández-Torre, K. Kośmider, J. Carrasco, M. V. Ganduglia-Pirovano and R. Pérez, *J. Phys. Chem. C*, 2012, **116**, 13584–13593.

30   M. Huang and S. Fabris, *J. Phys. Chem. C*, 2008, **112**, 8643–8648.

31   M. Nolan and G. W. Watson, *J. Phys. Chem. B*, 2006, **110**, 16600–16606.

32   M. Nolan, S. C. Parker and G. W. Watson, *Surf. Sci.*, 2006, **600**, 175–178.

33   Z. Wu, M. Li and S. H. Overbury, *J. Catal.*, 2012, **285**, 61–73.

34   T. Bunluesin, R. J. Gorte and G. W. Graham, *Appl. Catal. B Environ.*, 1998, **15**, 107–114.

35   Y. Chen, H. Wang, R. Burch, C. Hardacre and P. Hu, *Faraday Discuss.*, 2011, **152**, 121–133.

36   C. Schilling and C. Hess, *Top. Catal.*, 2017, **60**, 131–140.

37   A. Filtschew, K. Hofmann and C. Hess, *J. Phys. Chem. C*, 2016, **120**, 6694–6703.

38   Q. Wu, F. Zhang, P. Xiao, H. Tao, X. Wang, Z. Hu and Y. Lü, *J. Phys. Chem. C*, 2008, **112**, 17076–17080.

39   H.-X. Mai, L.-D. Sun, Y.-W. Zhang, R. Si, W. Feng, H.-P. Zhang, H.-C. Liu and C.-H. Yan, *J. Phys. Chem. B*, 2005, **109**, 24380–24385.

40   U. R. Pillai and S. Deevi, *Appl. Catal. A Gen.*, 2006, **299**, 266–273.

41   A. Laachir, V. Perrichon, A. Badri, J. Lamotte, E. Catherine, J. C. Lavalley, J. El Fallah, L. Hilaire, F. Le Normand, E. Quéméré, G. N. Sauvion and O. Touret, *J. Chem. Soc. Faraday Trans.*, 1991, **87**, 1601–1609.

42   D. A. Shirley, *Phys. Rev. B*, 1972, **5**, 4709–4714.

43   C. T. Nottbohm and C. Hess, *Catal. Commun.*, 2012, **22**, 39–42.

44   C. Schilling and C. Hess, *J. Phys. Chem. C*, 2018, **122**, 2909–2917.

45   M. Tinoco, S. Fernandez-Garcia, M. Lopez-Haro, A. B. Hungria, X. Chen, G. Blanco, J. A. Perez-Omil, S. E. Collins, H. Okuno and J. J. Calvino, *ACS Catal.*, 2015, **5**, 3504–3513.

46   C. Schilling, A. Hofmann, C. Hess and M. V. Ganduglia-Pirovano, *J. Phys. Chem. C*, 2017, **121**, 20834–20849.

47   J. P. Perdew, K. Burke and M. Ernzerhof, *Phys. Rev. Lett.*, 1996, **77**, 3865–3868.

48   T. Tabakova, F. Boccuzzi, M. Manzoli, J. W. Sobczak, V. Idakiev and D. Andreeva, *Appl. Catal. B Environ.*, 2004, **49**, 73–81.

49   H. Y. Kim and G. Henkelman, *J. Phys. Chem. Lett.*, 2013, **4**, 216–221.

50   S. Fuente, M. M. Branda and F. Illas, *Theor. Chem. Acc.*, 2012, **131**, 1190.

51   J.-C. Liu, Y.-G. Wang and J. Li, *J. Am. Chem. Soc.*, 2017, **139**, 6190–6199.

52   S. Link and M. A. El-Sayed, *J. Phys. Chem. B*, 1999, **103**, 8410–8426.

53   J. A. Hernández, S. A. Gómez, T. A. Zepeda, J. C. Fierro-González and G. A. Fuentes, *ACS Catal.*, 2015, **5**, 4003–4012.

54   M. Nolan, J. Fearon and G. Watson, *Solid State Ionics*, 2006, **177**, 3069–3074.

55   C. W. M. Castleton, J. Kullgren and K. Hermansson, *J. Chem. Phys.*, 2007, **127**, 244704.

56   Y. Gao, R. Li, S. Chen, L. Luo, T. Cao and W. Huang, *Phys. Chem. Chem. Phys.*, 2015, **17**, 31862–31871.

57   N. Ta, J. Liu, S. Chenna, P. A. Crozier, Y. Li, A. Chen and W. Shen, *J. Am. Chem. Soc.*, 2012, **134**, 20585–20588.

58   N. Yi, R. Si, H. Saltsburg and M. Flytzani-Stephanopoulos, *Energy Environ. Sci.*, 2010, **3**, 831.

59   X.-P. Fu, L.-W. Guo, W.-W. Wang, C. Ma, C.-J. Jia, K. Wu, R. Si, L.-D. Sun and C.-H. Yan, *J. Am. Chem. Soc., Just Accept. Manuscr. •*, , DOI:10.1021/jacs.8b09306.

60   Y. Lee, G. He, A. J. Akey, R. Si, M. Flytzani-Stephanopoulos and I. P. Herman, *J. Am. Chem. Soc.*, 2011, **133**, 12952–12955.

61   C. Schilling, M. V. Ganduglia-Pirovano and C. Hess, *J. Phys. Chem. Lett.*, 2018, **9**, 6593–6598.

62   G. N. Vayssilov, M. Mihaylov, P. S. Petkov, K. I. Hadjiivanov and K. M. Neyman, *J. Phys. Chem. C*, 2011, **115**, 23435–23454.

63   Z. V. Popović, Z. Dohčević-Mitrović, M. J. Konstantinović and M. Šćepanović, *J. Raman Spectrosc.*, 2007, **38**, 750–755.

64   Z. Dohčević-Mitrović, Z. V. Popović and M. Šćepanović, *Acta Phys. Pol. A*, 2009, **116**, 36–41.

65   M. Nolan, V. S. Verdugo and H. Metiu, *Surf. Sci.*, 2008, **602**, 2734–2742.

66   H. Y. Kim and G. Henkelman, *J. Phys. Chem. Lett.*, 2012, **3**, 2194–2199.

67   Q. Fu, A. Weber and M. Flytzani-Stephanopoulos, *Catal. Letters*, 2001, **77**, 87–95.

68   A. A. Gokhale, J. A. Dumesic and M. Mavrikakis, *J. Am. Chem. Soc.*, 2008, **130**, 1402–1414.

69   M. B. Watkins, A. S. Foster and A. L. Shluger, *J. Phys. Chem. C*, 2007, **111**, 15337–15341.

70   J. Vecchietti, A. Bonivardi, W. Xu, D. Stacchiola, J. J. Delgado, M. Calatayud and S. E. Collins, *ACS Catal.*, 2014, **4**, 2088–2096.